ISSN 2075-1087, Gyroscopy and Navigation, 2024, Vol. 15, No.2, pp. 28-38
Russian Text © The Author(s), 2024, published in Giroskopiya i Navigatsiya, 2024, No.2, pp. 46-65.

Real-time Calibration of Odometer in Integration with LiDAR and Gyroscope for Map-aided Positioning During GNSS Outages

Mohamed El-Tokhey[a], Mohamed Elhabiby[a], Tarek Hassan[a]*

[a]*Ain Shams University, Cairo, Egypt*

**e-mail: tarek.walid@eng.asu.edu.eg*

Received January 25, 2024; reviewed May 24, 2024; accepted June 27, 2024

Abstract: In recent research, significant efforts have focused on achieving dependable real-time positioning in challenging environments, which is a crucial aspect for the development of various Intelligent Transportation Systems (ITS) applications. Given the limitations of Global Navigation Satellite Systems (GNSS) in suburban and urban areas, where signal blockage is common, there is a growing need for an independent positioning system to provide accurate and continuous location data during GNSS disruptions. Previous studies have explored the combination of Light Detection and Ranging (LiDAR), gyroscopes, and odometer sensors for this purpose. This research builds upon that foundation by introducing a real-time calibration process for odometer readings, leveraging road maps and a road segmentation technique. To evaluate this method, real-world data collected from a moving vehicle was used, incorporating three five-minute simulated GNSS outages. These data were processed in a simulated real-time mode. The results from these tests are promising, showing notable improvements in navigation accuracy. Specifically, the application of the real-time calibration method led to an enhancement in positioning accuracy by 0.9m, 1.0m, and 0.2m for each of the GNSS outages, respectively, highlighting the critical role of this calibration process. The performance of the algorithm was improved during the second and third outages with the increased availability of line features. The proposed simpler LiDAR data processing algorithm could achieve mean positional errors of 1.8 m and 1.8 m, with maximum errors of 4.0 m and 3.8 m, respectively.

Keywords: navigation, odometer, LiDAR, gyroscope, ITS.

1. INTRODUCTION

For the past years, a lot of research projects have focused on how well navigation algorithms perform in suburban and urban environments. This interest is motivated by the ongoing development and deployment of Intelligent Transportation Systems (ITS) and the related applications that depend on the availability of navigation systems capable of consistently and accurately delivering positional solutions. These systems should be accurate enough to satisfy the requirements of ITS applications, which range from a few meters' accuracy in liability-critical applications to lane accuracy in safety-of-life applications. Collision-warning systems, emergency services management, and lane-keeping systems are examples of safety-of-life applications where undiscovered positional errors might threaten human life. On the other hand, liability-critical applications where undiscovered navigational errors can result in wrong legal and financial decisions include pay-per-use insurance, on-street parking, electronic toll collection, and road user charging [1, 2]. Some ITS applications require navigation systems that can monitor the environment continuously to adapt to the changing traffic scenarios while maintaining accuracy and continuity [3]. This includes the probability of occurrence of unacceptable situations (e.g., conflicts and collisions) which is important to be determined among other parameters in the navigation process.

Global Navigation Satellite Systems (GNSS) are unable to continuously provide navigational solutions in suburban and urban areas due to signal blockages that frequently occur. This makes it difficult to develop and deploy some ITS applications because their requirements are unmet. As a result, additional sensors are combined with GNSS receivers to provide continuous positioning solutions throughout GNSS outages. These can include odometers, digital cameras, 5G signals, ultrasonic, Inertial Measurement Units (IMUs), Radio Detection and Ranging (RADAR), and Light Detection and Ranging (LiDAR) [4–6]. This study integrates an odometer sensor with gyroscope and LiDAR sensors to provide continuous navigational solutions during GNSS outages.

Some studies in the literature proposed algorithms that fuse odometers with IMUs and LiDAR sensors. The study by [7] presented a real-time LiDAR-IMU-odometer system to provide navigation solutions by resolving the cost functions including the IMU and LiDAR residuals. In addition, loop closure and pose-graph optimization are used to reduce error accumulation. Over the tests that were run, the absolute positional errors varied from 0.92 m to 31.33 m. In [8], a similar integration was proposed using an error-state Kalman Filter (KF). The state estimation and the probability distribution obtained from the IMU measurements are utilized to assess the ground conditions. After that, the tightly coupled integration is optimized by adjusting the related parameters. Using this method on three different data sets achieved Root Mean Square (RMS) errors of 1.21%, 2.80%, and 2.60% of the travelled distances. In another approach [9], an extended KF is used to fuse the data from the three sensors after the point clouds acquired by LiDAR are matched with known point clouds using a point-to-plane Iterative Closest Point (ICP) technique. This method was proven to work well at straight paths and limited driving speeds (about 2 m/s). The study by [10] employed the Normal Distributions Transform (NDT) scan matching approach to enhance the pose estimations in the integration. The system was initialized by fusing the encoder and IMU data, and a robot was utilized to test the suggested technique. The positional error reached the 5-meter level at about 600 m running distance, and the cumulative angular error reached 15° while maintaining a running speed of 0.5 m/s. In another approach, [11] developed an iterated error-state KF to recursively correct the estimated state by generating new feature correspondences in each iteration. In order to avoid filter divergence over time, this technique used a robocentric formulation to represent the state in a local moving frame. Over the first 600m of outdoor testing, navigational errors were only a few meters, but beyond that, the errors significantly increased to exceed 25 m after the following 400 m. In the same context, in [12], the ICP algorithm is used for registration after skewed combined feature point clouds are generated. Ultra-Wideband (UWB) data is added to the IMU pose node as a one-dimensional over-edge constraint. When this technique was tested on the road, the positional error reached 5.78 m in only 85 m. Furthermore, a tightly coupled LiDAR-IMU integration employing a Gaussian particle filter was presented by [13]. Also, the same observations were loosely integrated using a rank KF in [14]. Both of these methods, developed for robots, had good accuracies for indoor limited distances. Calibration of odometer measurements was presented in previous works such as [15–17]. These self-calibration techniques relied on the existence of GNSS observations integrated with IMU and odometer measurements. However, GNSS observations are subjected to additional vulnerabilities in urban and suburban environments, which can affect the continuity and reliability of these calibration processes. Even with the reception of a sufficient number of GNSS signals in these environments, the accuracy and reliability of positional solutions cannot be guaranteed [18].

This contribution proposes a novel real-time calibration algorithm for odometer measurements relying on predefined road segments from maps. The technique is completely independent of GNSS observations to deliver reliable and continuous navigation during GNSS outages. LiDAR, gyroscope, and odometer measurements are combined employing line-based scan matching. Fault Detection and Exclusion (FDE) is used to identify and exclude the incorrectly matched lines between scans. In addition, the incorporated “road segmentation” process restrains the possible error accumulation and corrects the azimuth of the driving vehicle. The proposed method builds upon the assumption that vehicles are subjected to very small pitch and roll angles which is the usual case in paved roads, and so, they can be assumed zeros. The proposed real-time algorithm is tested using real trajectory data by introducing 5-minute GNSS outages. The remainder of this paper is structured as follows. A review of the used fusion algorithm is presented in Section 2. The proposed odometer real-time calibration technique is described in Section 3. The testing strategy used in this study is then described in Section 4. Later, Section 5 presents and discusses the test results to assess how well the employed algorithm performs. Finally, the conclusions of this contribution are given in Section 6.

2. REVIEW OF THE FUSION ALGORITHM

The proposed method in this study is an extension of the algorithm proposed by [19]. This fusion algorithm is reviewed in this section.

The necessary measurements in the first stage of the algorithm include LiDAR, gyroscope, and odometer measurements. These measurements are tied to the body frame represented by the vehicle’s forward direction as the Y-axis, transverse direction as the X-axis, and the vertical direction as the Z-axis.

The last position and azimuth obtained from GNSS are used as the initial conditions of the algorithm. The initial coordinates relative to the World Geodetic System 1984 (WGS84) datum are projected to the Universal Transverse Mercator (UTM) system for navigation purposes. The azimuth angle is defined as the clockwise angle measured from the north direction to the forward direction of the moving vehicle. This azimuth angle transforms coordinates from the X-Y-Z body frame (with its origin occupied by the LiDAR sensor after aligning the sensor axes shown on its base plate with the vehicle's body) to the local East-North-Up frame (with its origin as the UTM system origin) as will be described later. The initial azimuth angle of the moving vehicle is computed from the velocities derived from GNSS Doppler observations as $A = arctan(v_e/v_n)$, where v_e and v_n refer to the east and north velocities, respectively. Therefore, to ensure the accuracy of the computed azimuth, the vehicle should be moving rectilinearly without manoeuvre. It should be emphasized that the azimuth of non-moving vehicles cannot be initialized and the algorithm starts only after the vehicle moves. Once the algorithm is initialized, the vehicle can move or stop while the algorithm is running completely independent of GNSS observations.

The used integration algorithm adopts the line-based scan matching technique [20, 21]. This technique relies on the definition of the normal points in two successive scans (point clouds). The point where the detected line and the normal to the detected line from the LiDAR sensor intersect is known as the normal point. The location change of normal points from one frame to another is used to compute the position and heading change between these frames. As depicted in Figure 1, two parameters characterize the normal points for scans i and j; the polar range r and the polar angle θ. X_i and Y_i are the axes of frame i, while X_j and Y_j are the axes of frame j. The position changes, between the two scans in the body frame (i), are denoted Δx_i and Δy_i. ΔA refers to the anti-clockwise heading change from frame i to frame j.

Using the acquired LiDAR data, extracting lines starts by making a line from the first two points, and its polar parameters (i.e., r and θ) are calculated. Then, the following points are added while updating the polar parameters of the line after adding each point in a Least-Squares (LS) line estimation process. Points are added to the current line after satisfying the geometry and intensity conditions [19]. After extracting all lines, the availability of merging lines is checked to improve the efficiency of the following stages of the algorithm. For U number of lines, the lines (u and u^t) are merged if the following two conditions are satisfied:

$$r_l^u - r_l^{u'} \le r_{thres.} \quad (1)$$

$$\theta_l^u - \theta_l^{u'} \le \theta_{thres.} \quad (2)$$

where r_l^u and $r_l^{u'}$ denote the updated polar ranges of lines u and ut, while θ_l^u, $\theta_l^{u'}$ refer to their updated polar angles. $r_{thres.}$ and $\theta_{thres.}$ are predefined thresholds in both conditions.

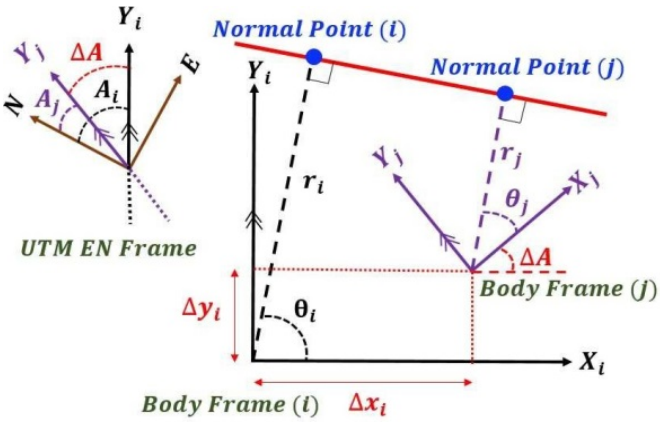

Fig. 1 The normal points and coordinate systems of two successive LiDAR frames

In the following stage, a search is performed to match the extracted lines in the current scan (j) to those in the previous scan (i). This is achieved with the help of odometer and gyroscope measurements by predicting the polar ranges and angles of lines in the current scan using the predicted changes in position and heading as follows:

$$r_{j|i} = r_i - (\Delta x_{odo} \cos\theta_i + \Delta y_{odo} \sin\theta_i) \quad (3)$$

$$\theta_{j|i} = \theta_i - \Delta A_{gyro} \quad (4)$$

where $r_{j|i}$ and $\theta_{j|i}$ are the predicted polar range and angle of the normal point. Δx_{odo} and Δy_{odo} denote the position changes in the X_i and Y_i directions obtained from the used odometer. ΔA_{gyro} refers to the directional change from the gyroscope readings. Odometers provide the vehicular speed in the moving direction (i.e., the Y_i direction), so, Δx_{odo} is assumed to be zero. Δy_{odo} can be calculated by multiplying the odometer speed by the measurement interval. It should be noted that $r_{j|i}$ and $\theta_{j|i}$ will be equal to r_j and θ_j in case of using ideal values of Δx_{odo}, Δy_{odo}, and ΔA_{gyro}.

A match is confirmed if the differences between the polar elements in the current scan (j) and the corresponding estimated ones ($j|i$) are within the search

space predefined thresholds for the polar ranges and angles ($\sigma_{r_{search}}$ and $\sigma_{\theta_{search}}$). These search spaces are assumed to account for the errors in odometer and gyroscope measurements that are used for the prediction of the polar ranges and angles in the following scan. This includes non-orthogonality, misalignment, scale factor, skidding, slipping, wheel diameter change ...etc. Following Equations 3 and 4, the linear relationship joining the relative navigational solution and the polar parameters for m number of matched lines is formed as follows:

$$\begin{bmatrix} r_{i_1}-r_{j_1} \\ r_{i_2}-r_{j_2} \\ \vdots \\ r_{i_m}-r_{j_m} \\ \theta_{i_1}-\theta_{j_1} \\ \theta_{i_2}-\theta_{j_2} \\ \vdots \\ \theta_{i_m}-\theta_{j_m} \end{bmatrix} = \begin{bmatrix} \cos\theta_{i_1} & \sin\theta_{i_1} & 0 \\ \cos\theta_{i_2} & \sin\theta_{i_2} & 0 \\ \vdots & \vdots & \vdots \\ \cos\theta_{i_m} & \sin\theta_{i_m} & 0 \\ 0 & 0 & 1 \\ 0 & 0 & 1 \\ \vdots & \vdots & \vdots \\ 0 & 0 & 1 \end{bmatrix} \begin{bmatrix} \Delta x_i \\ \Delta y_i \\ \Delta A_i \end{bmatrix} + e. \quad (5)$$

The previous relationship takes the parametric form, $l = G\hat{x} + e$, where l and $\hat{x}$ are the observations vector and the unknowns vector. G denotes the coefficient matrix, while e refers to the white noise vector $\begin{bmatrix} e_1 & e_2 & \cdots & e_{2_m} \end{bmatrix}^T$. Consequently, the LS solution of this system, with respect to the initial frame, is calculated as follows:

$$\begin{bmatrix} \Delta x_i \\ \Delta y_i \\ \Delta A_i \end{bmatrix} = (G^T W G)^{-1} G^T W l = S l \quad (6)$$

where W is the weight matrix of measurements and S represents the pseudo-inverse matrix mapping the observations space onto the unknown space. The weight of each pair of matched lines (i.e., the difference between their polar parameters) is assumed to be directly proportional to the number of points constituting each line in scans i and j. In addition, it is assumed to be inversely proportional to the normal distance from the LiDAR sensor to the line. This can be expressed mathematically as:

$$W = diag(W_1, W_2, ..., W_m, W_1, W_2, ..., W_m) \quad (7)$$

$$W_M = \frac{n_{i_m} + n_{j_m}}{D_M} \qquad M = 1, 2, ..., m \quad (8)$$

where W_M refers to the weight of line M, and D_M denotes the normal distance from the LiDAR sensor to line M. n_{i_M} and n_{j_M} are the number of points forming line Min frames i and j, respectively.

At least, two matched non-collinear lines are needed to get Δx_i and Δy_i, while only one line is required to get ΔA_i (see Figure 2). Any redundancy in the numberof matched lines is exploited to perform Fault Detection and Exclusion (FDE) in theposition domain using Solution Separation (SS) tests to detect the faulty matched lines between LiDAR scans [19].

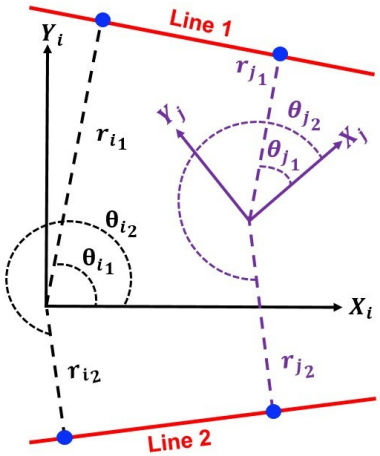

Fig. 2 An example of two matched lines in two consecutive epochs

The relative navigation solution is computed after eliminating the faulty matched lines. The obtained heading change is used to update the azimuth (A_i) of the moving vehicle, while the positional change is transformed from the body frame to the local frame (using the vehicle's azimuth) before updating the vehicle's position. The changes in the east direction (ΔE) and in the north direction (ΔN) can be derived as:

$$\begin{bmatrix} \Delta E_i \\ \Delta N_i \end{bmatrix} = \begin{bmatrix} \cos A_i & \sin A_i \\ -\sin A_i & \cos A_i \end{bmatrix} \begin{bmatrix} \Delta x_i \\ \Delta y_i \end{bmatrix} \quad (9)$$

The derived ΔE_i and ΔN_i values are used to update the position of the vehicle. The updated position and azimuth values are used as the initial values in the next epoch. It should be noted that the use of collinear matched lines causes solution singularity that affects the derived positional change. Therefore, to avoid this effect, the difference between the polar angles of the used lines should be less than a predefined threshold which can be assumed to be θ_{thres}. like the line merging stage. This threshold is applied directly with the parallel lines on the same roadside. On the other hand, with the parallel lines on opposite roadsides, an angle of 180° is added to this threshold before its applica-

tion to compensate for the difference in polar angles. If no relative solution is available due to the unavailability of two non-collinear matched lines, the heading change is obtained from the gyroscope, and the positional change is obtained from the odometer, assuming that Δx_i equals zero. The unavailability of line features can be caused by the lack of these features or by the existence of obstructing objects such as other vehicles, trees, pedestrians, ...etc.

The road segmentation process is used to avoid the accumulation of angular errors and correct the azimuth. The azimuth is only updated after ensuring that the vehicle moves without manoeuvre in the segment's forward direction. This can be inferred from the gyroscope measurements as described in [19]. If the difference between the current azimuth and the segment's azimuth (from the map) exceeds a predefined limit (ΔA_{limit}), the azimuth is updated to the preknown map segment azimuth.

3. THE PROPOSED REAL-TIME ODOMETER CALIBRATION

Odometers measure distances using a sensor and a gear-tooth wheel of ferromagnetic material. If the wheel moves, the sensor feels the change in the magnetic field between the sensor's permanent magnet and the wheel. The detected variations in flux level are transformed into output voltages. The frequency of these voltages is proportional to the frequency of the wheel. If the measured signal frequency (i.e., the counted number of teeth in one second) is denoted f_s, the measured odometer speed value (v_{odo}) canbe computed as [6]:

$$v_{odo} = \frac{2\pi r_v}{N_{tw}} f_s \qquad (10)$$

where N_{tw} is the number of teeth on the platform's wheel, while r_v is the radius of the wheel.

The measurement model of odometers is expanded in practice to include different error sources. This includes the wheel misalignment that is caused by the imperfect sensor mounting, relative to the axes of the vehicle, gyroscope, and LiDAR sensor. The effect of this error is systematic. Consequently, it can be treated by a prior calibration process and can be neglected in our measurement model. The major problem is the non-systematic errors that are caused by the unpredictable behavior of wheels due to external effects. The upper bound of these errors cannot be predicted, which represents a major problem while using odometers. These errors include wheel slipping, wheel skidding, and changes in the diameter of wheels due to variations in speed, pressure, temperature, and tread wear. Therefore, a scale factor for odometer measurements is needed according to the current wheel condition and environmental conditions. Then, Equation 10 is expanded so that the actual speed value (v^a_{odo}) can be expressed as:

$$v^a_{odo} = S_{odo} \frac{2\pi r_v}{N_{tw}} f_s + M_s + \epsilon_{odo} \qquad (11)$$

where S_{odo} is the introduced scale factor and M_s is the velocity error budget caused by the wheel misalignment due to the imperfect wheel and sensor mounting. The mechanical calibration process of M_s adjusts the angles of the wheels so that they are parallel to the vehicle's forward direction and to each other. ϵ_{odo} denotes the remaining non- systematic errors uncompensated by the introduced scale factor. This includes the non-systematic errors described above, in addition to the errors caused by the limited resolution of the odometer (i.e., the insensitivity to the fractional number of teeth). In our study, both M_s and ϵ_{odo} are assumed zeros.

In this stage of the proposed algorithm, a scale factor is computed to calibrate the subsequent odometer measurements. Each straight segment is given a unique identification number, and its corner coordinates are defined before navigating and running the algorithm (see Figure 3).

Fig. 3 Segmentation of roads on straight segments (shown in red color)

The rotation angle of the vehicle at each epoch (R_v), with respect to the forward direction of the road, is used in this real-time calibration process. To compute this rotation angle using LiDAR sensors, the initial assumption that buildings on roadsides are parallel to the forward direction is adopted. Usually, when GNSS solutions are unavailable, buildings exist on both roadsides indicating this scenario. The vehicle is confirmed to be moving in the segment's forward di-

rection only if two detected lines, at least, indicate this scenario; one with a polar angle between (–Ψ) and (+Ψ) and another one with a polar angle between (180°–Ψ) and (180°+Ψ), where Ψ is the value of R_v that can be neglected (see Figure 4). Otherwise, the obtained polar angles of the two lines indicate the value of R_v.

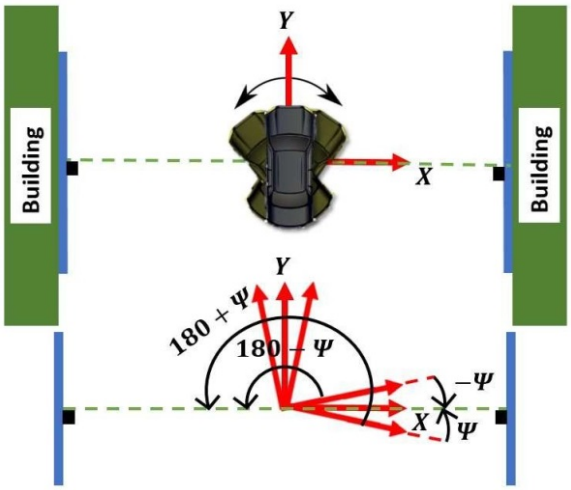

Fig. 4 The relationship between the vehicle's rotation angle of the vehicle and the detected linesrepresenting buildings

For each straight segment, the total running distance of the vehicle is computed as the sum of Δy_{odo} values. Therefore, the distance of this straight segment, see Figure 5, based on the measurements of odometer (L_{odo}) can be computed as:

$$L_{odo} = \sum_{u=1}^{U} \Delta y_{odo}^{u} \cos R_v^u \qquad (12)$$

where the superscript u denotes the epoch inside the straight segment, while (U) is the total number of epochs inside the segment z.

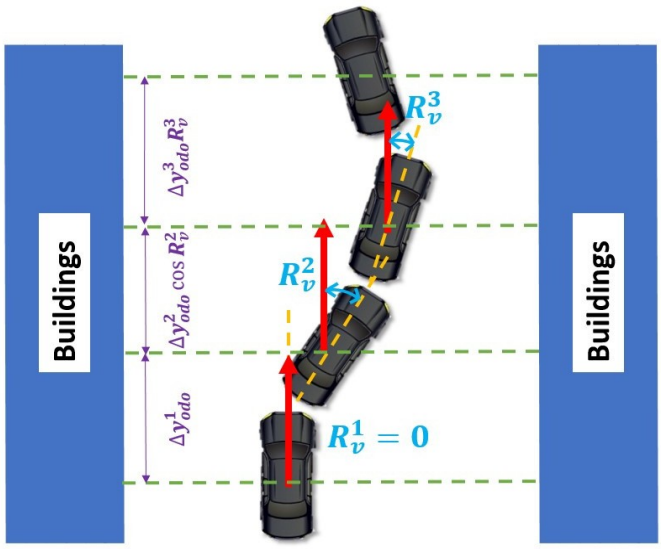

Fig. 5 The distance of a straight segment based on the proposed method

It should be noted that the assumption that the trajectory can be divided into small straight segments is valid in case of usinghigh-frequency observations. In our study, we use a 10Hz data frequency to increase the efficiency of the algorithm. L_{odo} is compared to the actual segment's straight distance defined from the map (L_{map}), as the computed positions of the vehicle are sufficient to identify the segment and know when the vehicle enters and exits this straight segment in the used map. A scale factor (S_{odo_z}) is computed to correct the measurements of the odometer in the following epochs such that:

$$S_{odo_z} = \frac{L_{map}}{L_{odo}}. \qquad (13)$$

After computing the scale factor from the first straight segment, it is used in the navigation process. Then, after passing another straight segment, another scale factor is computed. In this case, the scale factor used in the following navigation is updated to be the average of both scale factors. The same action is taken after passing additional straight segments (employing the moving average method) so that:

$$S_{odo} = \sum_{z=1}^{Z} \frac{S_{ozo_z}}{Z} \qquad (14)$$

where Z is the total number of passed straight segments and S_{odo_z} is the computed scale factor in segment z. It should be noted that scale factors should not change in short-time intervals, but they are updated in the algorithm to increase the sample used to compute the scale factor expectation. At any epoch, if the two building lines on both roadsides show different R_v values (i.e., not within a predefined threshold T_{Rv}), this indicates that their orientations are different. Therefore, the assumption that buildings on both roadsides are parallel to the forward direction of the road becomes invalid. In this case, scale factors are not computed inside segments with this condition. In this study, T_{Rv} is assumed to be 5°.

4. TESTING THE PRESENTED METHOD

In this section, the presented algorithm is tested using real-world data collected in Kingston-Ontario-Canada by a moving vehicle along the shown trajectory in Figure 6. The vehicle is equipped with LiDAR, gyroscope, and odometer sensors. The used LiDAR sensor is Velodyne Puck VLP-16 which has 30° vertical Field of View (FoV) with 2° resolution, 360° horizontal FoV with

0.1°–0.4° resolution, and 3 cm range precision [22]. The integrated VTI Micro-Electro-Mechanical-System (MEMS) gyroscope has 1°/*hr* short-term bias instability, 0.45°/√*hr* angular random walk, 2000 *ppm* scale factor, and ±100°/*s* output range precision (https://datasheetspdf.com/pdf/1413586/VTItechnologies/SCR1100-D02/1). The provided errors are with a confidence level of 99.7%. The number of teeth of the used odometer is 33. A NovAtel IMU-KVH1750 tactical-grade IMU is integrated with a dual-frequency GNSS receiver in a Precise Point Positioning (PPP)/IMU tightly-coupled mode to determine the reference positions of the vehicle. The measurements from the used LiDAR and odometer sensors are collected at a 10Hz rate, while the VTI MEMS gyroscope measurements are collected at a 20 Hz rate. Consequently, all collected measurements are synchronized at a 10 Hz rate and processed in a simulated real-time mode. The IMU-KVH1750 reference system can provide a data rate up to 200 Hz, but it is synchronized in real-time with the other sensors at a 10Hz rate for comparison and assessment purposes. All computed and compared coordinates are absolute coordinates relative to WGS84 datum and projected to the UTM system.

Sufficient GNSS observations were available during the test, which lasted for about 16 minutes. At least, six satellites were observed throughout the trajectory. The maximum number of observed satellites was 16, while the average number during the test was 12 satellites. However, to test the proposed algorithm, three GNSS outages are introduced in the trajectory (see Figure 6). Each of the three outages lasted for five minutes. The authors of this research developed software to process the gathered data according to the suggested algorithm.

As reviewed in Section 2, different parameters and thresholds are included in the algorithm. To assess the accuracy improvement after applying the real-time odometer calibration, the same parameters and thresholds adopted by [19] are used in this study. These parameters and thresholds are listed in Table 1.

Table 1 The parameters/ thresholds used in the appliedalgorithm

Parameter/Threshold	Value
$r_{thres.}$	10 *cm*
$\theta_{thres.}$	0.7°
$\sigma_{r_{search}}$	15 *cm*
$\sigma_{\theta s_{earch}}$	0.8°
ΔA_{limit}	10°
Ψ	5°

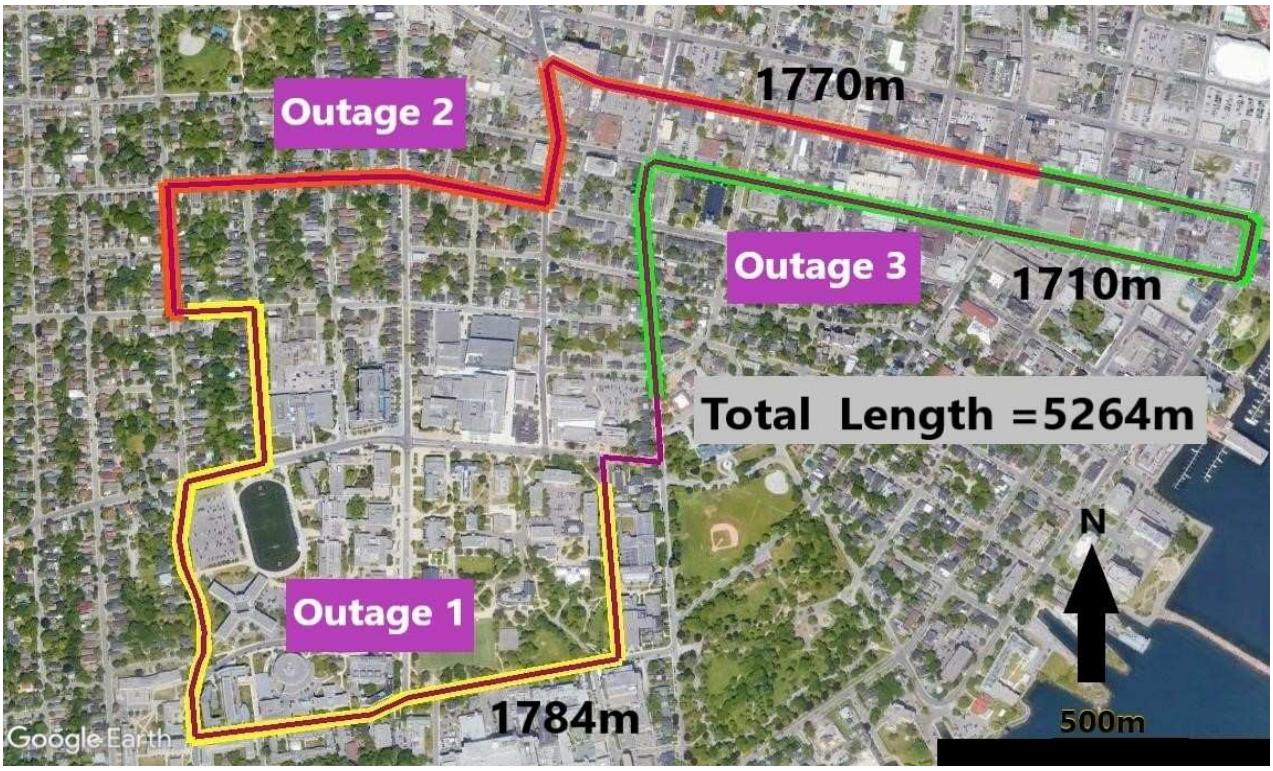

Fig. 6 The vehicle trajectory, shown in purple, and the three GNSS outages; the first outage in yellow, the second outage in red, and the third outage in green (Google Earth)

5. EFFECT OF ODOMETER CALIBRATION ON THE NAVIGATION ACCURACY

The results obtained after applying the presented method to the acquired data are presented and discussed in this section. Furthermore, the achieved navigation accuracies over the introduced GNSS outages are evaluated.

The number of extracted lines at each epoch primarily depends on the environment and the utilized algorithm. Open-sky areas are less opportune to the extraction process than urban and suburban environments. In the second and third outages, more lines could be extracted and matched. Also, the lack or the absence of extracted lines existed in some epochs, especially in the first outage. Generally, the mean numbers of matched lines in the second and third outages (15 and 14 lines) are more satisfactory than the mean number in the first outage (only 8 lines). The reason is the lower density of surroundings in the first outage. Figure 7 shows the number of detected, merged, and matched lines at each epoch over the three outages. In addition, Table 2 gives statistics of the number of the three line categories (i.e., extracted, merged, and matched) over the three GNSS outages.

Table 2. Statistics of the number of the three line categories over the three outages.

Outage Number	Lines Status	Min	Max	Mean
1	Extracted	0	79	26
	Merged	0	33	11
	Matched	0	30	8
2	Extracted	5	83	42
	Merged	4	42	20
	Matched	1	34	15
3	Extracted	4	101	38
	Merged	3	45	18
	Matched	1	34	14

The numbers of extracted and merged lines are not related to the calibration process, so, they were the same before and after the odometer calibration. However, the number of matched lines over each outage is affected by the calibration process. After applying the calibration algorithm, the mean number of matched lines decreased from 9 to 8 and from 16 to 15 in the first and second outages, while it increased from 13 to 14 in the third outage. To evaluate the linear accuracy after applying the proposed real- time calibration method, Table 3 shows the navigated versus the reference distancesin the three outages.

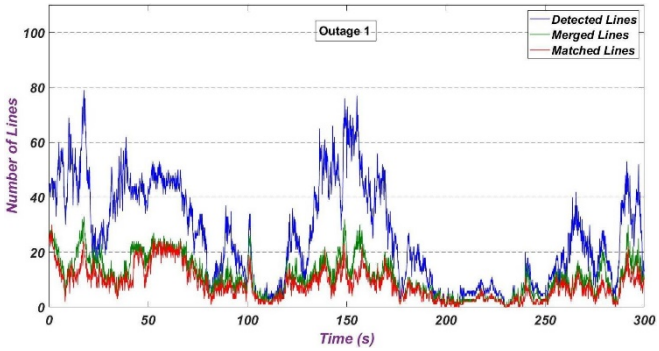

(a)

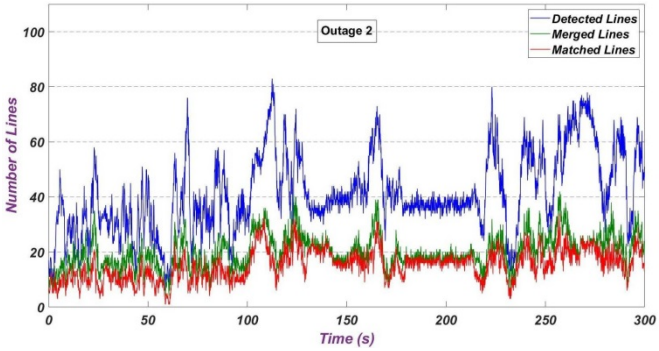

(b)

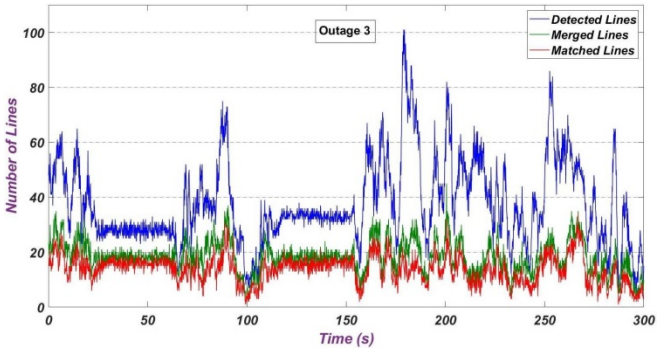

(c)

Fig. 7 The number of detected, merged, and matched lines in (a) the first outage (b) the secondoutage (c) the third outage

Table 3. The navigated versus the reference distances in the three outages before andafter odometer calibration

Outage Number	Navigated Distance (m)		Reference Distance (m)	Error (%)	
	Before	After		Before	After
1	1794.15	1789.8	1783.85	0.58	0.34
2	1761.9	1766.25	1770.35	0.48	0.23
3	1717.15	1715.15	1710.4	0.39	0.28

The results in Table 3 indicate promising improvements in the linear accuracies after applying the proposed algorithm with real-time calibration of odometer measurements. The ratios between the navigated distances after and before calibrating the odometer measurements were 0.9976, 1.0025, and 0.9988 for the three outages, respectively. These ratios emphasize the influence of the computed odometer scale factors (S_{odo}) on the navigation process. In the first outage, 5 straight segments were used in computing a scale factor of 0.9974, while 3 segments were used in the second and third outages to compute scale factors of 0.9978 and 0.9972, respectively. A standard test was conducted in the same trajectory by comparing the distances measured by the used odometer to the reference distances provided by the tactical-grade reference system. This is to evaluate the level of agreement between the resulting odometer scale factors in the algorithm and the reference scale factor in the test conditions. The reference scale factor was 0.9969 indicating an agreement with the computed scale factors in the algorithm (0.9974, 0.9978, and 0.9972) in the order of 0.05%, 0.09%, and 0.03%. Finally, the resulting navigational solutions are compared to the reference solutions after using the suggested algorithm. The discrepancies between the two solutions signify the horizontal errors that occurred at each epoch during the three outages. The horizontal error at each epoch is computed as $\sqrt{\Delta E^2 + \Delta N^2}$, where ΔE and ΔN are the discrepancies between the resulting navigational solution and the reference solution in the east and north directions, respectively. The computed errors give an indication of the navigational accuracy that can be attained by using the proposed approach for extended periods without GNSS solutions (see Figure 8). Table 4 provides statistics on these horizontal errors, including the maximum, mean, and RMS values (the numbers are rounded to the nearest 5 cm).

Table 4. Statistics of the horizontal errors after applying the proposed fusion algorithm over the three outages.

Outage Number	Max (m)	Mean (m)	RMS (m)
1	6.85	2.8	3.25
2	4.0	1.8	1.95
3	3.8	1.8	2.0

It can be deduced from Figure 8 and Table 4 that the proposed algorithm can provide a highly promising performance, particularly in rich environments where more line features can be extracted. This is evident from the results in the second and third outages, when the positional errors in the five minutes (300 seconds) reached 4.0 m and 3.8 m, respectively. In addition, the second outage had a mean error of 1.80 m with an RMS of 1.95 m, while the third outage had a mean error of 1.8 m with an RMS of 2.0 m. In the first outage, due to the lower density of surroundings, it was expected that the achieved performance would not be as good as it was during the other two outages. During this outage, the positional error reached 6.85 m, while the mean and RMS values were 2.8 m and 3.25 m, respectively. By comparing the obtained results to the results presented by [19], without applying the proposed real-time calibration method, significant positional accuracy improvements were found.

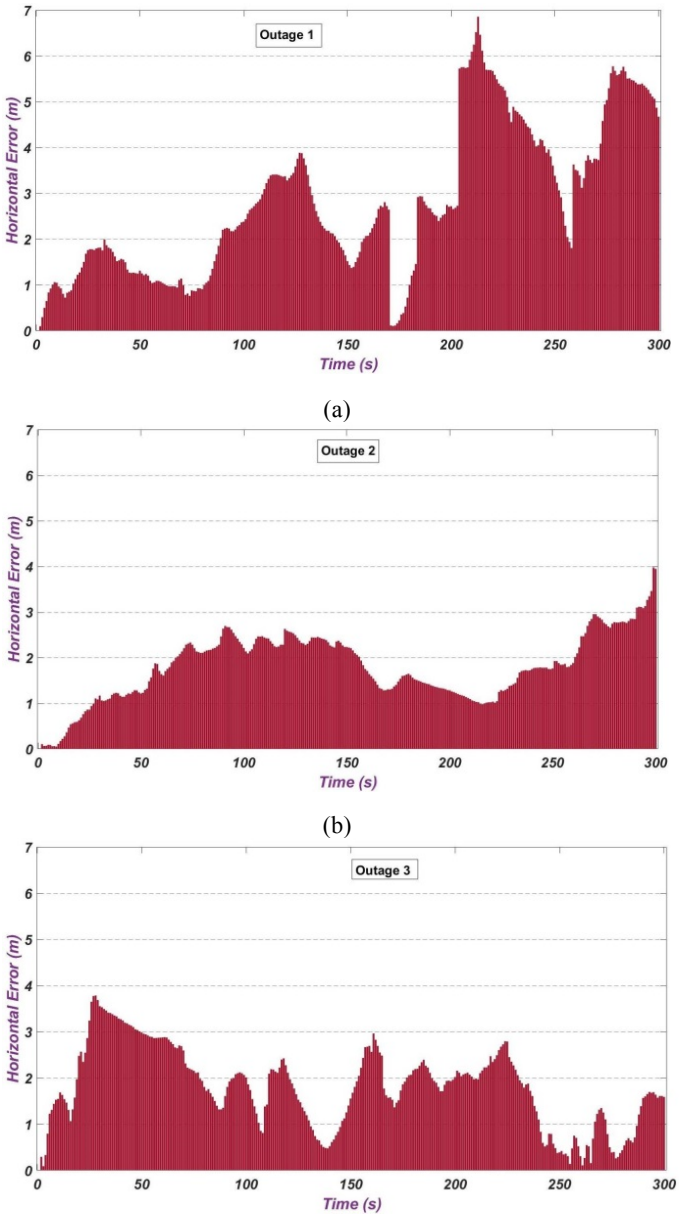

Fig. 8 The horizontal errors after applying the proposed fusion algorithm in (a) the first outage (b) the second outage (c) the third outage

Figure 9 shows the achieved improvement over the three outages (the difference between the positional errors without applying the proposed odometer calibration algorithm and the positional errors after applying it). In addition, Table 5 presents statistics of the achieved accuracy improvements after the real-time calibration of odometer measurements (the numbers are rounded to the nearest 5 cm).

Table 5. Statistics of the achieved accuracy improvements after applying the real-time calibration of odometer measurements

Outage Number	Max (m)	Mean (m)	RMS (m)
1	0.9	0.3	0.4
2	1.0	0.4	0.45
3	0.2	0.05	0.1

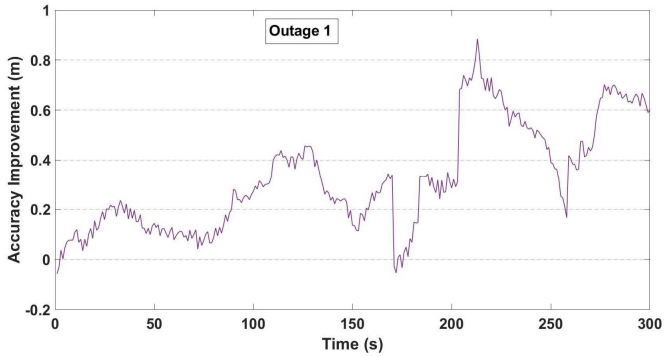

(a)

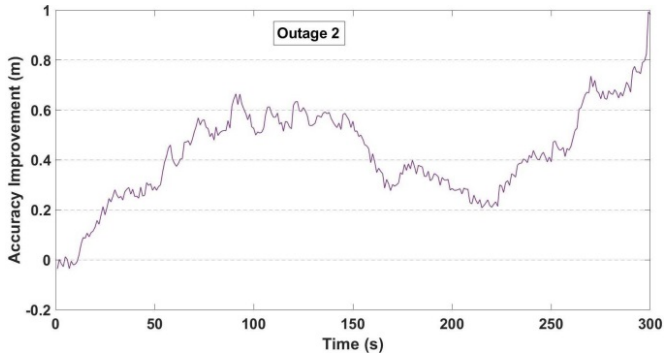

(b)

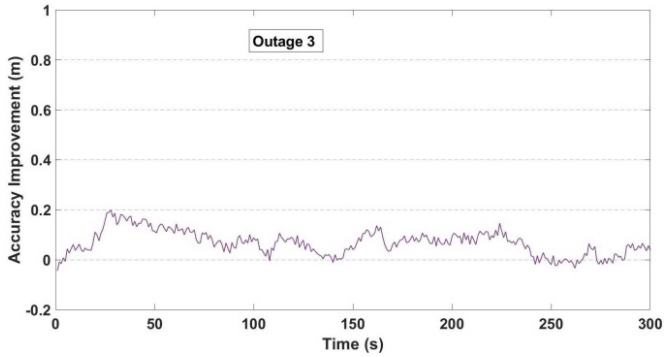

(c)

Fig. 9 The accuracy improvement after applying the real-time odometer calibration in (a) the first outage (b) the second outage (c) the third outage

Figure 9 and Table 5 show that the navigational accuracy improvement reached 0.9m, 1.0m, and 0.2m over the three GNSS outages. These numbers emphasizethe substantial influence of calibrating the odometer measurements on the obtained navigational solutions during GNSS outages.

CONCLUSIONS

This study introduces a novel real-time calibration method for odometer measurements, integrated into a real-time algorithm that combines LiDAR, gyroscopes, and odometers. This approach is designed to ensure uninterrupted navigation, especially during prolonged GNSS outages. The algorithm utilizes a line-based scan matching technique, tailored for vehicular navigation in ITS applications. It incorporates an FDE test to identify and discard mismatched lines between scans and employs a road segmentation process to limit potential accumulations of angular errors. Crucially, the algorithm includes a real-time updating feature for the calculated scale factor as part of the odometer real-time calibration algorithm.

The effectiveness of this method was evaluated using actual vehicle trajectory data, including three simulated five-minute GNSS outages. The data was processed using custom software developed by the researchers. The findings suggest that the proposed algorithm can deliver promising navigational performance, particularly in urban environments where more line features are available for matching. Notably, the algorithm's performance was improved during the second and third outages due to the increased availability of line features. Across these outages, the mean positional errors provided by the proposed simpler LiDAR data processing algorithm were recorded at 1.8 m and 1.8 m, with maximum errors of 4.0 m and 3.8 m, respectively. A significant enhancement in navigation accuracy was observed after calibrating the odometer measurements, with improvements of 0.9 m, 1.0 m, and 0.2 m noted across the three GNSS outages. These results underscore the effectiveness and robustness of the proposed real-time calibration method for odometer measurements in maintaining reliable navigation during GNSS outages.

FUNDING

This work was supported by ongoing institutional funding. No additional grants to carry out or direct this particular research were obtained.

CONFLICT OF INTEREST

The authors of this work declare that they have no conflicts of interest.

REFERENCES

1. GSA, Report on the Performance and Level of Integrity for Safety and Liability Critical Multi-applications, European Global Navigation Satellite Systems Agency, 2015.
2. GSA, Technical Analysis of New Paradigms Increasing EGNSS Accuracy and Robustness in Vehicles, European Global Navigation Satellite Systems Agency, 2015.
3. Ninalalov, I., Merkuryev, I., Kubryak, O., and Astakhov, S., Methods for Improv- ing the Accuracy of an Autonomous Orientation and Navigation System Based on Micromechanical Gyroscopes and Optoelectronic Sensors. In 2022 29th Saint Petersburg International Conference on Integrated Navigation Systems (ICINS), 2022, pp. 1-2.
4. Wang, Z., Wu, Y., and Niu, Q., Multi-sensor Fusion in Automated Driving: A Survey, *IEEE Access*, 2019, 8, pp. 2847-2868.
5. Hassan, T., El-Mowafy, A., and Wang, K., A Review of System Integration and Current Integrity Monitoring Methods for Positioning in Intelligent Transport Systems, IET Intelligent Transport Systems, 2021, 15, 1, pp. 43-60.
6. Golovan, A.A., INS/odometer integration: positional approach. *Gyroscopy and Navigation*, 2021, 12, pp. 186-194. https://doi.org/10.1134/S2075108721020048
7. Yang, J.-C., Lin, C.-J., You, B.-Y., Yan, Y.-L., and Cheng T.-H., RTLIO: Real- Time LiDAR-Inertial Odometry and Mapping for UAVs, *Sensors*, 2021, 21, 3955.
8. Zhao, Z., Zhang, Y., Shi, J., Long, L., and Lu, Z., Robust Lidar-Inertial Odometry with Ground Condition Perception and Optimization Algorithm for UGV, *Sensors*, 2022, 22, 7424.
9. Zhang, S., Guo, Y., Zhu, Q., and Liu, Z., Lidar-IMU and Wheel Odometer Based Autonomous Vehicle Localization System, In 2019 Chinese Control and Decision Conference (CCDC), 2019, pp 4950-4955.
10. Zhou, B., Tang, Z., Qian, K., Fang, F., and Ma, X., A Lidar Odometry for Outdoor Mobile Robots Using NDT Based Scan Matching in GPS-denied Environ- ments, In 2017 IEEE 7th Annual International Conference on CYBER Technology in Automation, Control, and Intelligent Systems (CYBER), 2017, pp. 1230-1235.
11. Qin, C., Ye, H., Pranata, C.E., Han, J., Zhang, S., and Liu, M., LINS: A LiDAR-Inertial State Estimator for Robust and Efficient Navigation, In 2020 IEEE International Conference on Robotics and Automation (ICRA), 2020, pp. 8899-8906.
12. Zhang, C., Ma, X., and Qin, P., LiDAR-IMU-UWB-Based Collaborative Localization, *World Electric Vehicle Journal*, 2022, 13, 2, p. 32.
13. Zhen, W., Zeng, S., and Scherer, S., Robust Localization and Localizability Esti- mation with a Rotating Laser Scanner, In 2017 IEEE International Conference on Robotics and Automation (ICRA), 2017, pp. 6240-6245.
14. Jiang, P., Chen, L., Guo, H., Yu, M., and Xiong, J., Novel Indoor Positioning Algo- rithm Based on LiDAR/Inertial Measurement Unit Integrated System, International Journal of Advanced Robotic Systems, 2021, 18, 2, 1729881421999923.
15. Jiang, L., Bai-gen, C., Jian, W., and Tao, T., Grey Theory Based Odometer Scale Factor Calibration Method for Integrated Navigation System, In 2009 Second International Conference on Intelligent Computation Technology and Automation, 2009, Vol. 3, pp. 507-510.
16. Li, L., Sun, H., Yang, S., Ding, X., Wang, J., Jiang, J., Pu, X., Ren, C., Hu, N., and Guo, Y., Online Calibration and Compensation of Total Odometer Error in an Integrated System, *Measurement*, 2018, 123, pp. 69-79.
17. Wu, Y., Goodall, C., and El-Sheimy, N., Self-calibration for IMU/Odometer Land Navigation: Simulation and Test Results, In Proceedings of the 2010 International Technical Meeting of The Institute of Navigation, 2010, pp. 839-849.
18. Hassan, T., Fath-Allah, T., Elhabiby, M., Awad, A., and El-Tokhey, M., Detection of GNSS no-line of sight signals using LiDAR sensors for intelligent transportation systems. Survey Review, 2022, 54(385), pp. 301-309.
19. Hassan, T., Fath-Allah, T., Elhabiby, M., Awad, A., and El-Tokhey, M., A real- time algorithm for continuous navigation in intelligent transportation systems using LiDAR-Gyroscope-Odometer integration, *Journal of Applied Geodesy*, 2023, 17(1), pp. 65-77.
20. Borges, G.A. and Aldon, M.-J., Line Extraction in 2D Range Images for Mobile Robotics, *Journal of Intelligent and Robotic Systems*, 2004, 40, 3, pp. 267-297.
21. Soloviev, A., Bates, D., and Van Graas, F., Tight Coupling of Laser Scanner and Inertial Measurements for a Fully Autonomous Relative Navigation Solution, *Navigation*, 2007, 54, 3, pp. 189-205.
22. Velodyne LiDAR, VLP-16 User Manual, 63-9243 Rev. E, Velodyne LiDAR, Inc, 2019.